Journal of Materials Chemistry C

PAPER

View Article Online
View Journal | View Issue

Cite this: J. Mater. Chem. C, 2019, 7, 3342

Dual-mode color tuning based on upconversion core/triple-shell nanostructure†

Lei Lei, ‡[a] Xiaoru Dai,‡[a] Yao Cheng, *[b] Yuansheng Wang, [b] Zhen Xiao[a] and Shiqing Xu*[a]

Received 31st October 2018,
Accepted 9th February 2019

DOI: 10.1039/c8tc05467c

rsc.li/materials-c

Manipulating the upconversion (UC) emission color by externally applied fields allows access to a range of novel applications. Although such controls based on the multi-color UC nanocrystals (NCs) have previously been reported, it is still a challenge to construct a multi-mode responsive system that can enable multifunctionality within one single nanostructure. Herein, an integrated core/triple-shell nanostructure, in which the different activators are spatially separated, is applied for a dual-mode manipulation of the UC emission color. The 3-photon dominant UC emission intensity of the Tm^{3+} ions is enhanced more than that of the 2-photon counterpart of the Er^{3+} ions by increasing the excitation power, leading to an excitation power induced color variation. Moreover, the UC emission intensity of the Er^{3+} activators in the core exhibit a thermal quenching effect, while that of the Tm^{3+} ions in the second-shell show near-zero thermal quenching in the visible region, which contributes to the temperature dependent color change. Upon tuning the emission color by means of appropriate co-doping in the core, a series of power/thermal dual-mode responsive multi-color UC NCs are achieved, which endows the UC nanostructure with a bi-functionality that can find potential applications in temperature sensing and anti-counterfeiting fields.

Introduction

Benefiting from the abundant and characteristic excited state levels of lanthanide ions (Ln^{3+}), Ln^{3+}-activated upconversion NCs with multi-color emissions have attracted significant attention owing to their potential applications in diverse fields, such as imaging,[1–3] optical multiplexing,[4,5] temperature sensing,[6,7] as well as anti-counterfeiting[8–12] and display.[13–15] The different color emissions are fundamentally determined by the lanthanide activator ions as well as the chemical composition or crystal structure of the host.[16–19] However, a lot of exciting research has also demonstrated that the manipulation of emission colors can be realized by adjusting external conditions including the electronic and magnetic conditions, temperature, and excitation wavelength/pulse width/power density,[20–26] through which many novel functions for the UC NCs can be further derived from one single UC nanostructure. In this regard, multifunctionality can be achieved for a single elaborate UC nanostructure when different external stimuli are employed, which is of high demand in many circumstances.[27,28]

As an anti-Stokes process, UC can generate one high energy photon by absorbing two or more photons with low energy. The n value in the power law of UC ($I \propto P^n$, where I is the UC emission intensity, P is the excitation power and n is the number of required pumping photons) is highly related to the location of the energy level. For instance, the green and red emissions of Er^{3+} and Ho^{3+} ions are generally attributed to a two-photon UC, while the blue emission of the Tm^{3+} ions are ascribed to three and four-photon UC.[29–32] Theoretically, the spectral profiles of UC systems, where the emissions ascribed to different n values are combined, can be manipulated by simply tuning the excitation power owing to their disparate power-dependent rate of variation for the luminescent intensity, since emissions related to a high n value are enhanced faster than those with a low n value on increasing the excitation power. For example, on continuously modulating the excitation power, the UC emission color of $NaGdF_4$:Yb/Er@$NaGdF_4$@$NaGdF_4$:Yb/Tm@$NaGdF_4$ NCs is tuned from green to white[33] while that of $NaGdF_4$:Yb/Tm/Er@$NaGdF_4$:Eu@$NaYF_4$ NCs is changed from green to cyan to white and to red.[34] Such results are considered to be very suitable for anti-counterfeiting applications.[35,36] Compared to commercial invisible inks that exhibit a single emission color under UV excitation, UC NCs

[a] College of Materials Science and Engineering, China Jiliang University, Hangzhou 310018, P. R. China. E-mail: shiqingxu@cjlu.edu.cn
[b] CAS Key Laboratory of Design and Assembly of Functional Nanostructures, and Fujian Key Laboratory of Nanomaterials, Fujian Institute of Research on the Structure of Matter, Chinese Academy of Sciences, Fuzhou, Fujian, 350002, P. R. China. E-mail: chengyao@fjirsm.ac.cn

† Electronic supplementary information (ESI) available. See DOI: 10.1039/c8tc05467c

‡ Lei Lei and Xiaoru Dai contributed equally to this work.

with a remote and dynamically controlled UC emission color variation are more secure for application in the anti-counterfeiting field.

Recently, a very interesting negative thermal quenching effect, *i.e.*, an increase in UC emission intensity with the increase in temperature, was observed in lanthanide-doped fluoride NCs.[37–39] Through the combination of this negative thermal quenching effect with normal thermal quenching *via* an elaborate core/shell nanostructure design, the manipulation of the UC emission color could be realized by means of temperature variation.

It is noteworthy that for both the scenarios stated above, core/shell nanostructures play a crucial role in realizing the manipulation of the emission color with different external stimuli. This inspires us to design a core/triple-shell nanostructure, which allows the simultaneous control of the UC emission color *via* excitation power and environmental temperature. Importantly, such a design can enable dual functionality within single nanostructure, *e.g.*, temperature sensing and anti-counterfeiting. As shown in Scheme 1, two kinds of activators with different n values are chosen for the excitation power response, while the spatial separation of the two activators *via* core/triple-shell architecture is considered for the thermal response.

As a proof-of-concept, taking $NaErF_4$, $NaErF_4$:5Yb or $NaErF_4$:2Eu as core NCs, uniform and monodisperse core@$NaYF_4$@$NaYbF_4$:0.5Tm@$NaYF_4$ core/shell/shell/shell (named as Er@3S, ErYb@3S and ErEu@3S corresponding to the employed $NaErF_4$, $NaErF_4$:5Yb and $NaErF_4$:2Eu as the core, respectively) NCs are prepared by an epitaxial growth method. With increasing the excitation power, the UC emission intensity of the Tm^{3+} ions in the blue region is enhanced more than that of Er^{3+} ions, which results in the emission color of Er@3S NCs to change from red to mauve, the emission color of ErYb@3S NCs changes from orange to royal-purple and that of ErEu@3S NCs changes from green to indigo. With an increase in the temperature from 293 to 413 K, the UC emission intensity of the activators in the core-only NCs increases and decreases after coating with a thick shell. As a result, the emission color of the Er@3S NCs changes from red to purple, the emission color of ErYb@3S NCs changes from yellow to cyan and that of ErEu@3S NCs changes from green to blue. Moreover, our results reveal that these nanosystems exhibit good temperature sensing properties owing to the thermally coupled energy levels of Er^{3+} and Tm^{3+} ions.[40,41] These power/thermal dual-mode responsive multi-color UC NCs have potential applications in multimodal bio-imaging, anti-counterfeiting, temperature sensing and information storage fields.

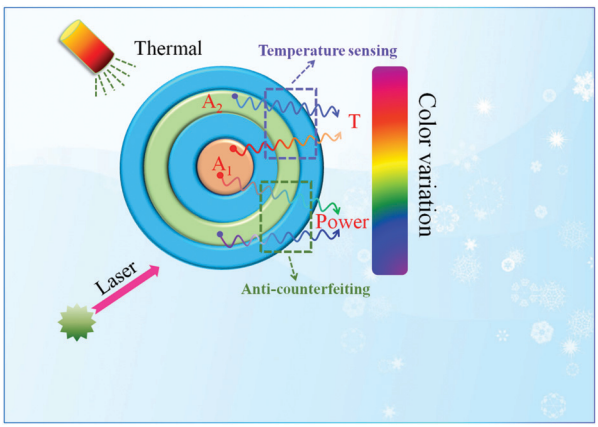

Scheme 1 Schematic illustration of dual-mode manipulation of the UC emission color by constructing a core/shell architecture. A_1 represents activator with n_1 and A_2 represents activator with n_2.

Experimental

Materials

All chemicals were of analytical grade and were used as received without further purification. Deionized water was used throughout. Ytterbium acetate hydrate ($Yb(Ac)_3{\cdot}xH_2O$, 99.9%), erbium acetate hydrate ($Er(Ac)_3{\cdot}xH_2O$, 99.9%), yttrium acetate hydrate ($Y(Ac)_3{\cdot}xH_2O$, 99.9%), thulium acetate hydrate ($Tm(Ac)_3{\cdot}xH_2O$, 99.9%), sodium acetate ($NaAc{\cdot}3H_2O$, 99.995%), ammonium fluoride (NH_4F, $\geq$98%), 1-octadecene (ODE, 90%) and oleic acid (OA, 90%) were supplied by Sigma Aldrich. Cyclohexane and absolute ethanol were purchased from Sinopharm Chemical Reagent Company.

Synthesis of nanocrystals

The lanthanide-doped core–multishell NCs are synthesized by a layer-by-layer epitaxial growth process. The detailed synthesis procedure is provided in the ESI.†

Synthesis of ligand-free nanoparticles

The as-prepared OA-capped nanoparticles were dispersed in a mixed solution of ethanol (1 mL) and HCl (0.2 M; 1 mL). The mixture was sonicated for 5 min and collected by centrifugation. Subsequently, the resulting products were washed with ethanol/H_2O three times.

Preparation of patterns for thermally-assisted color variation

Stamps were prepared by carving designed patterns on round oaks with a diameter of 2 cm. The surfaces of the stamps were dipped in the corresponding OA-capped NCs-containing cyclohexane solution and then stamped on normal A4 paper.

Preparation of luminescent ink for writing

The ink was prepared by dissolving 10 mg ligand-free ErEu@3S NCs in commercial invisible ink bought from Tianjin Ink Factory. The transparent pen (F10) for writing was bought from SIKIB Company.

Characterizations

X-ray diffraction (XRD) analysis was carried out with a powder diffractometer (Bruker D8 Advance) with a Cu-K_α (λ = 1.5405 Å) radiation. The morphology and scanning transmission electron microscopy (STEM) of the products were characterized by a field emission transmission electron microscopy (TEM, FEI Tecnai G^2 F20) equipped with an energy dispersive X-ray spectroscope (EDS, Aztec X-Max 80T). Temperature-dependent UC emission

spectra and decay curve measurements were carried out on an Edinburgh Instruments FLS920 spectrofluorimeter equipped with an adjustable laser diode (980 nm) and a temperature control stage. For the temperature-dependent characterization, the samples were kept at a certain temperature for about 10 min without changing other experimental conditions. The 980 nm laser for illuminating photographs was connected with a beam expander to obtain a large beam size of about 2.5 cm in diameter.

Results and discussion

The reported $NaLnF_4$-based (Ln = lanthanide) core/shell NCs with a hexagonal phase generally exhibit a three-dimensional morphology of hexagonal prisms[42,43] whose projection could exhibit different shapes, such as a hexagon from the top direction and rectangle-like from the side direction. To visualize the growth of the as-prepared NCs in three dimensions, planes of the specimens on the TEM grids are modified by tuning the polarity of the dispersant through the addition of appropriate amounts of ethanol to the as-prepared NCs-containing cyclohexane solutions. As shown in Fig. 1a–p, all the samples of $NaErF_4$:2Eu core, $NaErF_4$:2Eu@$NaYF_4$ core/shell (ErEu@S), $NaErF_4$:2Eu@$NaYF_4$@$NaYbF_4$:0.5Tm core/shell/shell (ErEu@2S) and ErEu@3S NCs exhibit a hexagonal nanoprism shape. High-resolution TEM images of these NCs reveal their single crystalline structure, and lattice fringes with a *d*-spacing of 0.513 nm and 0.297 nm correspond to the top (100) and side (110) faces, respectively (Fig. 1e–l). By growing the shells in a layer-by-layer fashion, the mean sizes of the top faces increase from 16 nm to 30 nm, while that of the lateral ones increase from 20 nm to 39 nm (Fig. S1, ESI†), indicating that the shells are coated on the core in three dimensions. STEM-HAADF images, which are sensitive to the atomic number, further verify the successful growth of shells out of the core NCs (Fig. 1q–t).[44,45]

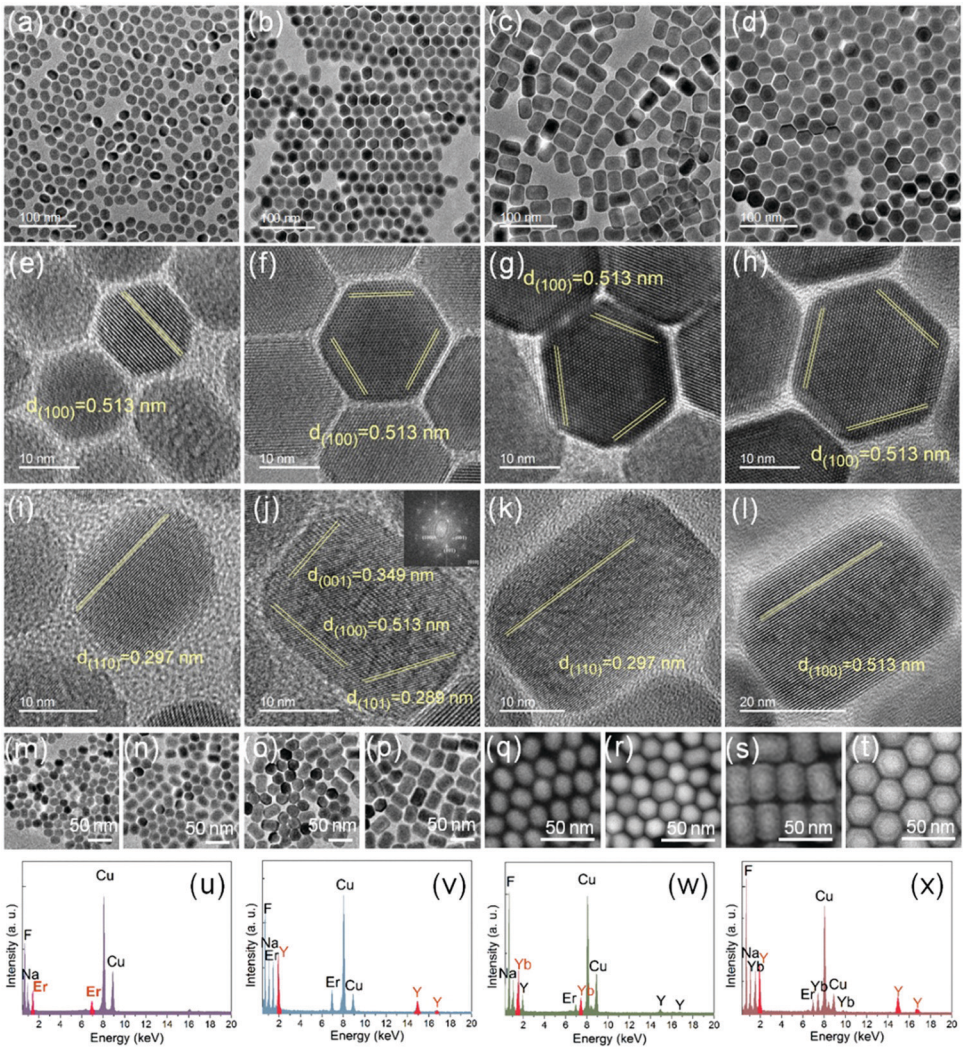

Fig. 1 TEM images of $NaErF_4$:2Eu core (a), $NaErF_4$:2Eu@$NaYF_4$ core/shell (b), $NaErF_4$:2Eu@$NaYF_4$@$NaYbF_4$:0.5Tm core/shell/shell (c) and ErEu@3S core/shell/shell/shell (d) NCs dissolved in cyclohexane solution. Top (e–h) and side (i–l) HRTEM images of (a–d), respectively. Inset of (j) is the corresponding Fourier transform diffraction pattern. (m–p) are TEM images of (a–d) dissolved in a mixture of ethanol and cyclohexane. (q–t) and (u–x) are respectively STEM-HAADF images and EDS spectra of (a–d).

EDS results reveal the element categories are consistent with those designed in the corresponding NCs (Fig. 1u–x). XRD patterns of the as-prepared samples (Fig. S2, ESI†) match well with the hexagonal $NaErF_4$ phase (JCPS No. 27-0689) and no extra impurity peaks were detected.

As shown in Fig. 2a, both characteristic emissions of Er^{3+} and Tm^{3+} ions are clearly observed for the Er@3S, ErYb@3S and ErEu@3S samples under 980 nm laser excitation. The core/shell structure has been widely applied to improve the UC emission intensity of the activators in the core and obtain novel UC properties by interstitial ions assisted energy migration processes.[46–48] As shown in Fig. S3 (ESI†), under the same excitation power, the green to red ratio of the Er^{3+} ions in $NaErF_4$@$NaYbF_4$ NCs is higher than that of $NaErF_4$@$NaYF_4$. This probably due to the existence of energy transfer from the Yb^{3+} ions in the shell to the Er^{3+} ions in the core *via* the Yb^{3+}:$^2F_{5/2}$ → Er^{3+}:$^4I_{11/2}$ energy level followed by enhanced green UC emission (Fig. S4, ESI†). For the core/triple-shell products in this study, the inner $NaYF_4$ layer is applied to separate activators in the core and the third layer spatially to inhibit deleterious cross-relaxation and energy transfer from Yb^{3+} in the shell to Er^{3+} in the core (Fig. 2b). Benefiting from the surface passivation effects, the UC emission intensities of the NCs with a shell layer are higher than the corresponding core NCs (Fig. S5, ESI†).[49,50] Moreover, the UC emission intensity of the Tm^{3+} ions is enhanced much more than that of the Er^{3+} ions after coating with an outer $NaYF_4$ layer, suggesting the outer $NaYF_4$ layer mainly contributes to an improvement in the emission intensity of the Tm^{3+} activators. Power dependent luminescence studies reveal n values for the $^1D_2$ → $^3F_4$ (452 nm), $^1G_4$ → $^3H_6$ (479 nm), $^4S_{3/2}$ → $^4I_{15/2}$ (545 nm) and $^4F_{9/2}$ → $^4I_{15/2}$ (660 nm) transitions are 3.25, 2.33, 1.91 and 2.45, respectively (Fig. 2c). The Tm^{3+}: $^1G_4$ → $^3F_4$ transition, which is located at ~660 nm, is clearly observed in $NaGdF_4$@$NaYbF_4$:0.5Tm@$NaGdF_4$ NCs (Fig. S6, ESI†), and hence we infer that the three-photon UC processes of the $^4F_{9/2}$ → $^4I_{15/2}$ transition can

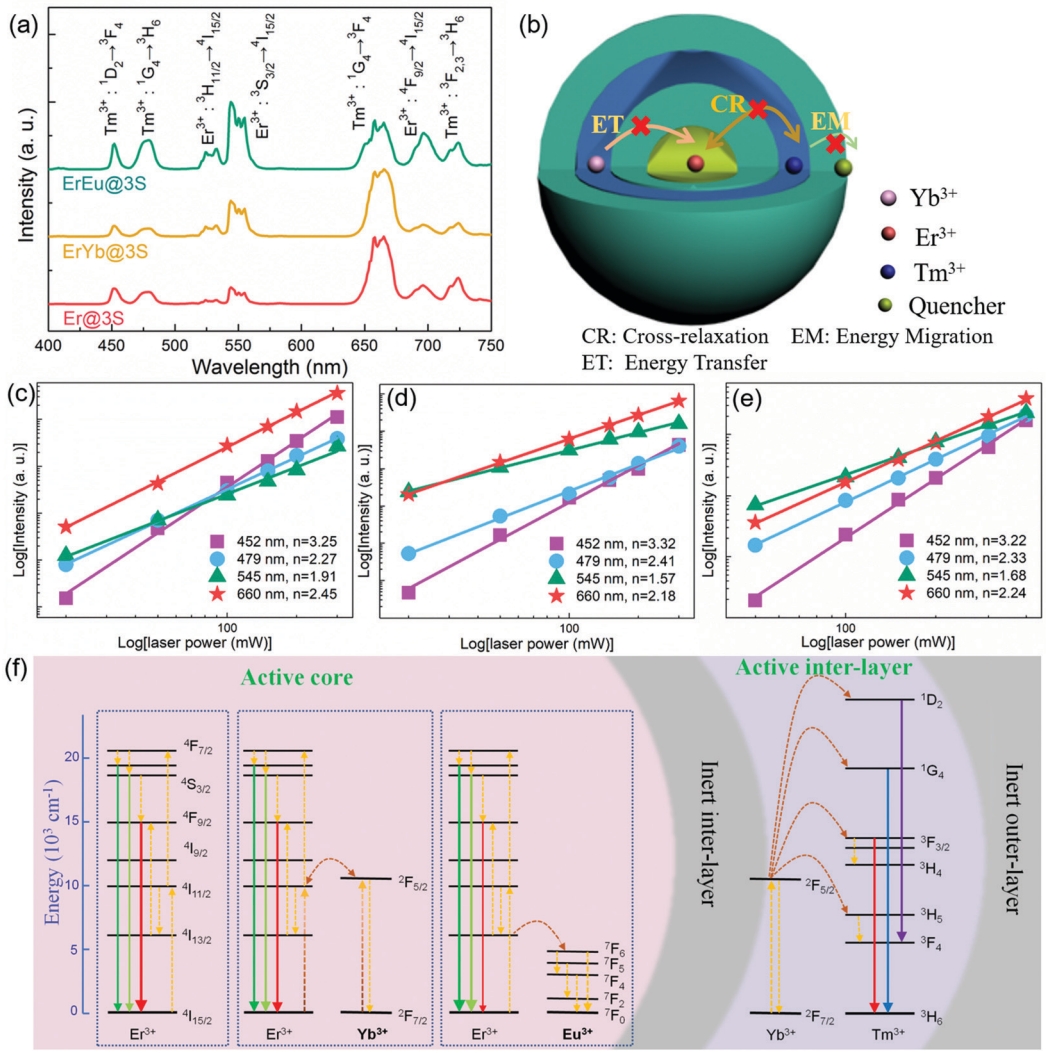

Fig. 2 (a) UC emission spectra of Er@3S, ErYb@3S and ErEu@3S NCs under 980 nm laser excitation. (b) Schematic illustration of the core/triple-shell structure. Double logarithmic plots of pump power *versus* the upconversion emission intensity of Er^{3+} (545 nm, 660 nm) and Tm^{3+} (452 nm and 479 nm) in the Er@3S (c), ErYb@3S (d) and ErEu@3S (e) NCs. (f) Proposed energy transfer mechanism in the related core/triple-shell NCs.

be attributed to the mixing of the radiative $^1G_4 \rightarrow {}^3F_4$ transition.[51] Owing to the high non-radiative relaxation possibility of the $^4S_{3/2} \rightarrow {}^4F_{9/2}$ and $^4I_{11/2} \rightarrow {}^4I_{13/2}$ processes,[52,53] a strong red emission of the Er^{3+} ions is observed. On doping 5 mol% Yb^{3+} or 2 mol% Eu^{3+} ions as new energy trapping centers into the $NaErF_4$ layer of the Er@3S NCs, the green to red intensity ratio increases,[54] however, the n values for the above transitions are only slightly changed (Fig. 2a, d and e). Doping Yb^{3+} ions into the $NaErF_4$ core facilitates the energy transfer from Er^{3+}:$^4I_{11/2}$ to Yb^{3+}:$^2F_{5/2}$ and then to the Er^{3+}:$^4I_{11/2}$ again, while doping Eu^{3+} ions benefits the depopulation of the Er^{3+}:$^4I_{13/2}$ energy level, both of which result in the enhanced relative green UC emission intensity of the Er^{3+} activators.[54] The related energy transfer mechanisms in these core/triple-shell NCs are shown in Fig. 2f.

According to the UC power law, the power dependent UC emission intensity ratio for the different emissions can be estimated by the following equation:

$$I_1/I_2 = P^{n_1}/P^{n_2} = P^{(n_1 - n_2)} \quad (1)$$

where P is the excitation power, n_1 and n_2 are the number of pumping photons required for the different transitions. Hence, the trend in the relative emission intensity variation is highly dependent on the n value difference between the related transitions. As expected in the present research systems, the emission color changes from red to mauve with an increase in the excitation power from 0.5 to 5 W, which is due to the different RGB variation rates (Fig. 3a). Similarly, the emission color changes from orange to royal-purple with an increase in the excitation power from 0.4 to 1.9 W for the ErYb@3S sample, while the output color changes from green to indigo with an increase in the excitation power from 0.5 to 2 W for the ErEu@3S sample (Fig. 3b and c). These results reveal that co-doping activators with different n values is a very effective strategy to manipulate the UC emission color by simply tuning the excitation power. It should be noted that the initial relative emission intensity between Er^{3+} and Tm^{3+} ions is very important for achieving the remarkable color variation *via* excitation power tuning. As shown in Fig. S7 (ESI†), on decreasing the emission intensity ratio of Tm^{3+} to Er^{3+} ions greatly by decreasing the particle size of ErEu@3S, the output color is difficult to tune owing to the very weak emission intensity of Tm^{3+} ions at higher powers. Such power dependent variation in emission color may be further amplified by combining with the plasmon, which has been proven to be able to realize the emission color control by selectively increasing either the local electric field for the enhancement of the absorption or the radiative decay rate.[55–57]

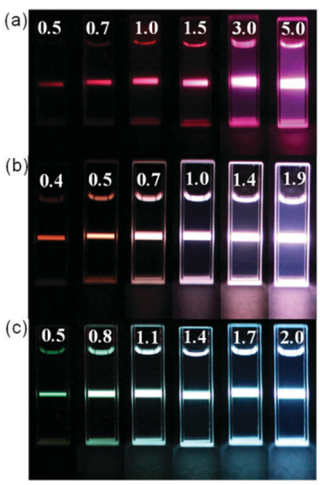

Fig. 3 Excitation-power dependent digital photographs of Er@3S (a), ErYb@3S (b) and ErEu@3S (c) NCs, respectively. The unit of excitation power is W.

It has been reported that lanthanide-doped fluoride UC NCs exhibit a negative thermal quenching effect owing to the decreased energy migration possibility from activators to surface defects at higher temperatures.[38,39] The distance between the activators and the surface defects increases with increasing shell layers, which could suppress the above energy transfer process (Fig. 4a). Hence, the different variation trends of Er^{3+} in the core and Tm^{3+} in the third layer are actualized through coating shells to selectively inhibit this surface-related energy migration process. Evidently, the UC emission intensity of Er^{3+} in the core decreases greatly, but the blue emission region of Tm^{3+} in the third layer remains almost unchanged with an increase in the temperature from 293 to 413 K (Fig. 4b–d). As shown in Fig. S8 (ESI†), the UC emission intensity of $NaErF_4$@$NaYF_4$ core/shell NCs remains almost unchanged with an increase in the temperature while its intensity begins to decrease evidently after coating another two layers of $NaYbF_4$:Tm@$NaYF_4$, which further reveals that the temperature dependency of the UC luminescence can be modified by tuning the shell layers. Although the relative UC emission intensity of Tm^{3+} and Er^{3+} is highly related to the excitation power, their variation trends *versus* temperature in the Er@3S NCs are almost independent of the excitation power (Fig. S9, ESI†). The decrease in emission intensity of Er^{3+} is attributed to the increased non-radiative relaxation possibility at a higher temperature, which is known as thermal quenching. The luminescence decay curves of Er@3S NCs reveal that the lifetime of Tm^{3+}:$^1G_4$ remains almost keep unchanged while that of Er^{3+}:$^4S_{3/2}$ and $^4F_{9/2}$ increases gradually with an increase in the temperature from 293 K to 413 K (Fig. 4e–g). The detailed calculation for the lifetimes are shown in the ESI.† The lifetime of the excited state energy level is highly related to the local electron depopulation pathway. With an increase in the temperature, the lattice expansion reduces the cross relaxation possibility between the Er^{3+} ions ($^4F_{7/2} + {}^4I_{11/2} \rightarrow {}^4F_{9/2} + {}^4F_{9/2}$) and decreases the energy transfer efficiency from the activators to the interfacial defects, which results in an increased lifetime of the Er^{3+} ions.[39] As a result of the suppression of the above cross-relaxation process, the lifetime of $^4S_{3/2}$ increases to more than that of $^4F_{9/2}$ and the ratio of red to green decreases from 5.02 to 4.18 with an increase in the temperature from 293 K to 413 K (Fig. S10, ESI†). For the situation with a low doping content of Tm^{3+} ions in a thin two-dimensional space, the above two effects do not affect the local electron depopulation pathway, which results in the variation trend of life-time to be consistent with that of UC emission intensity.

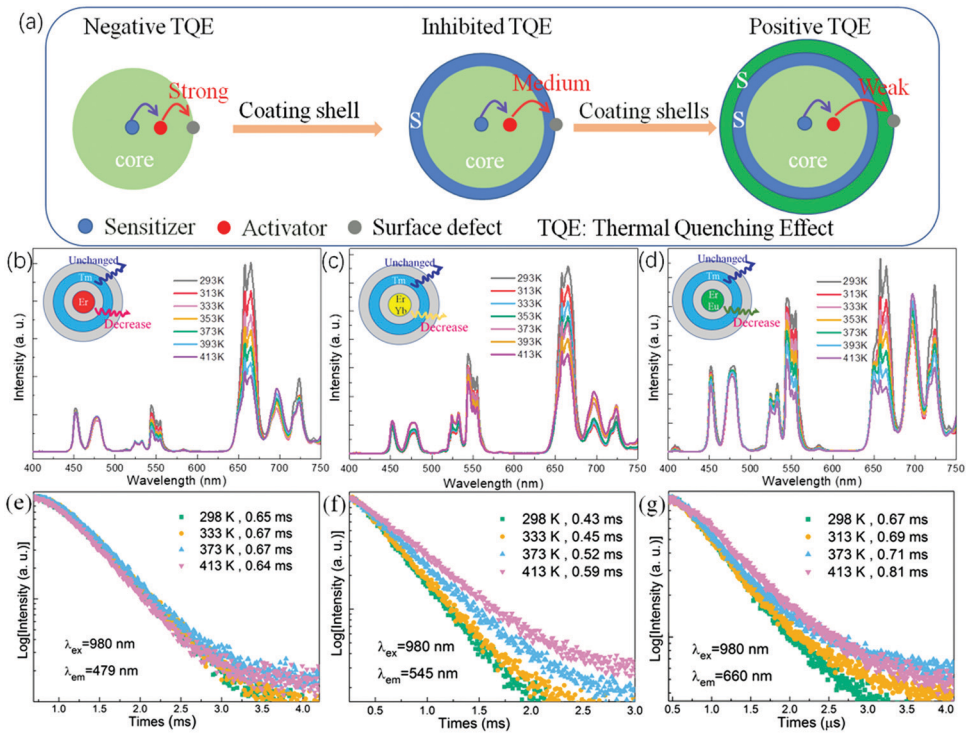

Fig. 4 (a) Schematic illustration for the inhibition of the surface-related effects through coating shells. Temperature dependent UC emission spectra of Er@3S (b), ErYb@3S (c) and ErEu@3S (d) NCs. Note that the "unchanged" in the insets represent the blue visible region that remains almost unchanged. UC decay curves of (e) Tm^{3+}:$^1G_4$ (λ_{em} = 479 nm), (f) Er^{3+}:$^4S_{3/2}$ (λ_{em} = 545 nm) and (g) $^4F_{9/2}$ (λ_{em} = 660 nm) in Er@3S NCs.

To visualize the temperature dependent color variation for the core/triple-shell NCs in our study, different patterns were prepared by brushing the NCs-containing solutions on oaks with the designed patterns and then painting on a normal A4 paper. Evidently, with an increase in the temperature from 293 to 413 K, the pattern painted with the Er@3S NCs changes from red to purple on fixing the excitation power to 2.5 W (Fig. 5a), the pattern prepared by ErYb@3S NCs changes from yellow to cyan at an excitation power of 0.8 W (Fig. 5b), while the pattern prepared by ErEu@3S NCs switches from green to blue at an excitation power of 1.2 W (Fig. 5c). It should be noted that the activator with the relatively stronger emission intensity should be doped into the core to actualize thermal-induced multi-color emissions. Based on the thermally induced color variation, a macroscopic temperature range could be evaluated.

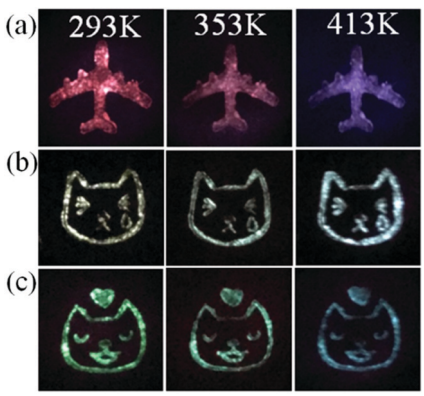

Fig. 5 (a) Digital photographs of the patterns painted by Er@3S (a), ErYb@3S (b) and ErEu@3S (c) NCs-containing inks at different temperatures under 980 laser illumination.

As a crucial thermodynamic parameter, the temperature significantly affects the breeding of biological cells as well as the therapeutics of diseases. UC NCs have potential application for *in situ* and real-time temperature sensing by connecting bio-tissues with surface-modified NCs. Herein, the temperature sensing properties based on the thermally coupled $^2H_{11/2}$/$^4S_{3/2}$ energy levels of Er^{3+} and $^3F_2$/$^3H_4$ energy states of Tm^{3+} in the core/triple-shell NCs were analyzed. As shown in Fig. 6a, based on the Boltzmann distribution theory, the fluorescence intensity ratio (FIR_G) of the $^2H_{11/2} \rightarrow {}^4I_{15/2}$ ($\sim$525 nm) to $^4S_{3/2} \rightarrow {}^4I_{15/2}$ ($\sim$545 nm) transition in Er@3S sample is expressed by the following equation:

$$FIR_G = I_{525}/I_{545} = C\exp\left(-\frac{\Delta E}{k_B T}\right) + A \quad (2)$$

where C and A are constants, ΔE represents the energy gap between the $^2H_{11/2}$ and $^4S_{3/2}$ states, k_B and T are the Boltzmann constant and absolute temperature, respectively.[58,59] Similarly, the fluorescence intensity ratio (FIR_R) of I_{696}/I_{658} *versus* T is well fitted by the above equation as well (Fig. 6b) except that ΔE represents the energy gap between the $^3F_{2,3}$ and $^3H_4$ states of the Tm^{3+} ions. The relative temperature sensitivity (S_R) is calculated by the following equation:

$$S_R = \frac{1}{FIR} \times \frac{d(FIR)}{dT} \quad (3)$$

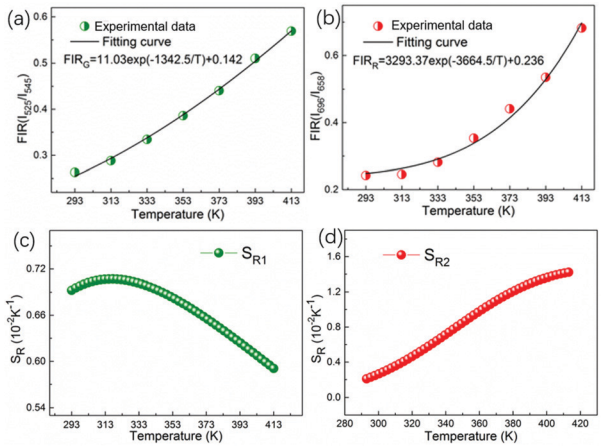

Fig. 6 Dependence of FIR values on temperature in Er@3S NCs: (a) I_{525}/I_{545} and (b) I_{696}/I_{658}. The fitting curves are also provided. (c) and (d) are the dependence of relative sensitivities on absolute temperature corresponding to (a) and (b), respectively.

As shown in Fig. 6c and d, the maximum S_{R1} and S_{R2} are 0.71 K^{-1} at 315 K and 1.42% K^{-1} at 413 K for FIR$_G$ and FIR$_R$, respectively. For the ErEu@3S sample, the maximum S_{R1} and S_{R2} are 0.48 K^{-1} at 357 K and 1.33% K^{-1} at 413 K for FIR$_G$ and FIR$_R$, respectively (Fig. S11, ESI†). For the ErYb@3S sample, the maximum S_{R1} and S_{R2} are 0.67 K^{-1} at 322 K and 1.53% K^{-1} at 413 K for FIR$_G$ and FIR$_R$, respectively (Fig. S12, ESI†). All of the above temperature sensing properties are comparable to most UC nano-systems.[60–62] Importantly, this dual-mode temperature sensing feature allows the signal selection for higher accuracy within the different temperature regions, which cannot be achieved by a single-mode system.

With the rapid development of world economic trade, fake commodities have become more and more serious in the modern society, which forced researchers to develop novel anti-counterfeiting technology with high security.[63] To reveal the possible application of the NCs in the present research for anti-counterfeiting, a dual-mode fluorescent ink was prepared by dissolving the ligand-free ErEu@3S NCs in a commercial invisible ink, and then '100' in Arabic numerals was written on a banknote of China. As shown in Fig. 7 and Fig. S13 (ESI†), the hand-written '100' is invisible under sunlight, while the blue '100' is observed clearly under 365 nm UV lamp illumination. It should be noted that the observed yellow '100' pattern is attributed to the applied anti-counterfeiting label by the government. Moreover, a bright green hand-written '100' is observed under 980 nm laser excitation, and the emission color changes to indigo with an increase in the excitation power (Fig. 7e). These results reveal that the core/triple-shell NCs with real-time and dynamic multi-color modulation characteristics are very suitable for high-security anti-counterfeiting application.

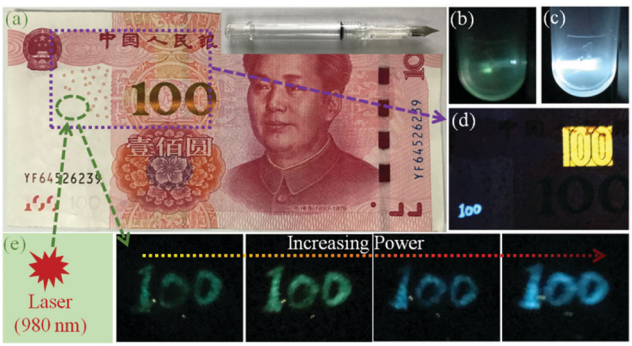

Fig. 7 (a) Normal banknote of China with hand-written Arabic numeral of '100' in the green circle region. Inset is the pen. Photographs of the as-prepared ink under 980 nm laser excitation at low (b) and high (c) power. (d) Photograph of the purple square region under 365 nm UV lamp illumination. (e) Photographs of the green circle region with an increase in the 980 nm laser excitation power.

Conclusions

In conclusion, different kinds of core/triple-shell NCs were successfully prepared by a layer-by-layer epitaxial growth process. Our results reveal that the UC emission intensity of Tm^{3+} ions was enhanced more than that of Er^{3+} ions on increasing the excitation power, leading to the excitation power induced color variation. In addition, the UC emission intensity of the Er^{3+} activators in the core exhibit a thermal quenching effect, while that of Tm^{3+} ions in the second-shell show near-zero thermal quenching in the visible region, contributing to the temperature dependent color change. The present researched dual-mode systems exhibit potential applications in temperature sensing with high accuracy and anti-counterfeiting with superior security. More importantly, we believe that this general strategy for the dual-mode manipulation of UC emission color given in this study may initiate widespread interest in multi-mode responsive systems aiming for multi-functionality in a single nanostructure.

Conflicts of interest

There are no conflicts to declare.

Acknowledgements

This work was supported by the Zhejiang Provincial Natural Science Foundation of China (No. LD18F050001, LY17E020007, LY18E020009); National Natural Science Foundation of China (No. 51702306).

References

1 J. Zhou, Z. Liu and F. Li, *Chem. Soc. Rev.*, 2012, **41**, 1323.
2 H. Dong, L. D. Sun, L. D. Li, R. Si, R. Liu and C. H. Yan, *J. Am. Chem. Soc.*, 2017, **139**, 18492.
3 H. Dong, S. R. Du, X. Y. Zheng, G. M. Lyu, L. D. Sun, L. D. Li, P. Z. Zhang, C. Zhang and C. H. Yan, *Chem. Rev.*, 2015, **115**, 10725.
4 G. Chen, H. Qiu, P. N. Prasad and X. Chen, *Chem. Rev.*, 2014, **114**, 5161.

5 L. Zhou, R. Wang, C. Yao, X. M. Li, C. L. Wang, X. Y. Zhang, C. J. Xu, A. J. Zeng, D. Y. Zhao and F. Zhang, *Nat. Commun.*, 2015, **6**, 6938.
6 D. Q. Chen, Z. Y. Wan, Y. Zhou, X. Z. Zhou, Y. L. Yu, J. S. Zhong, M. Y. Ding and Z. G. Ji, *ACS Appl. Mater. Interfaces*, 2015, **7**, 19484–19493.
7 Z. M. Cao, X. T. Wei, L. Zhao, Y. H. Chen and M. Yin, *ACS Appl. Mater. Interfaces*, 2016, **8**, 34546–34551.
8 X. W. Liu, Y. Wang, X. Y. Li, Z. G. Yi, R. R. Deng, L. L. Liang, X. J. Xie, D. Loong, S. Y. Song and D. Y. Fan, *et al.*, *Nat. Commun.*, 2017, **8**, 899.
9 P. Li, Q. Peng and Y. D. Li, *Adv. Mater.*, 2009, **21**, 1945.
10 Y. L. Liu, K. L. Ai and L. H. Lu, *Nanoscale*, 2011, **3**, 4804.
11 L. Lei, D. Q. Chen, C. Li, F. Huang, J. J. Zhang and S. Q. Xu, *J. Mater. Chem. C*, 2018, **6**, 5427.
12 W. J. Yao, Q. Y. Tian, J. Liu, Q. W. Xue, M. X. Li, L. Liu, Q. Lu and W. Wu, *Nanoscale*, 2017, **9**, 15982.
13 F. Wang, Y. Han, C. S. Lim, Y. Lu, J. Wang, J. Xu, H. Chen, C. Zhang, M. Hong and X. G. Liu, *Nature*, 2010, **463**, 1061.
14 Z. Yin, H. Li, W. Xu, S. Cui, D. Zhou, X. Chen, Y. Zhu, G. Qin and H. Song, *Adv. Mater.*, 2016, **28**, 2518.
15 Y. Wang, K. Z. Zheng, S. Y. Song, D. Y. Fan, H. J. Zhang and X. G. Liu, *Chem. Soc. Rev.*, 2018, **47**, 6473.
16 F. Wang and X. G. Liu, *J. Am. Chem. Soc.*, 2008, **130**, 5642.
17 G. Z. Ren, S. J. Zneg and J. H. Hao, *J. Phys. Chem. C*, 2011, **115**, 20141.
18 L. Lei, S. J. Zhang, H. Xia, Y. Tian, J. J. Zhang and S. Q. Xu, *Nanoscale*, 2017, **9**, 5718–5724.
19 Z. Zhuo, Y. S. Liu, D. J. Liu, P. Huang, F. L. Jiang, X. Y. Chen and M. C. Hong, *Chem. Sci.*, 2017, **8**, 5050.
20 J. H. Hao, Y. Zhang and X. H. Wei, *Angew. Chem., Int. Ed.*, 2011, **50**, 6876.
21 Y. X. Liu, D. S. Wang, J. X. Shi, Q. Peng and Y. D. Li, *Angew. Chem., Int. Ed.*, 2013, **52**, 4366.
22 P. Chen, H. Jia, Z. Zhong, J. Han, Q. Guo, J. Zhou, X. Liu and J. R. Qiu, *J. Mater. Chem. C*, 2015, **3**, 8794.
23 D. D. Li, Q. Y. Shao, Y. Dong and J. Q. Jiang, *J. Phys. Chem. C*, 2014, **118**, 22807.
24 H. Xia, L. Lei, W. Q. Hong and S. Q. Xu, *J. Alloys Compd.*, 2018, **757**, 239.
25 B. Chen, Y. Liu, Y. Xiao, X. Chen, Y. Li, M. Y. Li, X. S. Qiao, X. P. Fan and F. Wang, *J. Phys. Chem. Lett.*, 2016, **7**, 4916.
26 R. R. Deng, F. Qin, R. F. Chen, W. Huang, M. H. Hong and X. G. Liu, *Nat. Nanotechnol.*, 2015, **10**, 237.
27 F. F. Wang, D. Zhai, C. T. Wu and J. Chang, *Nano Res.*, 2016, **9**, 1193.
28 Y. J. Ding, X. X. Zhang, H. Zhu and J. J. Zhu, *J. Mater. Chem. C*, 2014, **2**, 946.
29 M. Pang, X. S. Zhai, J. Feng, S. Y. Song, R. P. Deng, Z. Wang, S. Yao, X. Ge and H. J. Zhang, *Dalton Trans.*, 2014, **43**, 10202.
30 H. Y. Li, Q. W. Huang, Y. B. Wang, K. Chen, J. Xie, Y. Pan, H. Q. Su, X. J. Xie, L. Huang and W. Huang, *J. Mater. Chem. C*, 2017, **5**, 6450.
31 J. Shen, G. Y. Chen, T. Y. Ohulchanskyy, S. J. Kesseli, S. Buchhlolz, Z. P. Li, P. N. Prasad and G. Han, *Small*, 2013, **9**, 3213.
32 W. Shao, G. Y. Chen, T. Y. Ohulchanskyy, C. H. Yang, H. Agren and P. N. Prasad, *Nanoscale*, 2017, **9**, 1934.
33 M. Hu, D. D. Ma, C. C. Liu, J. Wang, Z. X. Zhang and L. J. Meng, *J. Mater. Chem. C*, 2016, **4**, 6975.
34 C. Zhang, L. Yang, J. Zhao, B. H. Liu, M. Y. Han and Z. P. Zhang, *Angew. Chem., Int. Ed.*, 2015, **54**, 11531.
35 Y. M. Wang, X. T. Tian, H. Zhang, Z. R. Yang and X. B. Yin, *ACS Appl. Mater. Interfaces*, 2018, **10**, 22445.
36 M. X. Li, W. J. Yao, J. Lin, Q. Y. Tian, L. Liu, J. Ding, Q. W. Xue, Q. Lu and W. Wu, *J. Mater. Chem. C*, 2017, **5**, 6512.
37 Q. Y. Shao, G. T. Zhang, L. L. Ouyang, Y. Q. Hu, Y. Dong and J. Q. Jiang, *Nanoscale*, 2017, **9**, 12132.
38 X. S. Cui, Y. Cheng, H. Lin, F. Huang and Y. S. Wang, *Nanoscale*, 2017, **9**, 13794.
39 L. Lei, J. N. Xia, Y. Cheng, Y. S. Wang, G. X. Bai, H. Xia and S. Q. Xu, *J. Mater. Chem. C*, 2018, **6**, 11587.
40 S. Balabhadra, M. L. Debasu, C. D. S. Brites, R. A. S. Ferreira and L. D. Carlos, *J. Phys. Chem. C*, 2017, **121**, 13962.
41 W. Xu, X. Y. Gao, L. J. Zheng, Z. G. Zhang and W. W. Cao, *Sens. Actuators, B*, 2012, **173**, 250.
42 H. Wang, W. Lu, T. Zeng, L. Rao and S. Zeng, *Nanoscale*, 2013, **6**, 2855.
43 H. Wang, Z. Yi, L. Rao and S. Zeng, *J. Mater. Chem. C*, 2013, **1**, 5520–5526.
44 X. M. Li, D. K. Shen, J. P. Yang, C. Yao, R. C. Chen, F. Zhang and D. Y. Zhao, *Chem. Mater.*, 2013, **25**, 106.
45 K. A. Abel, F. C. Boyer, C. M. Andrei and F. Veggel, *J. Phys. Chem. Lett.*, 2011, **2**, 185.
46 Q. Q. Su, S. Y. Han, X. J. Xie, H. M. Zhu, H. Y. Chen, C. K. Chen, R. S. Liu, X. Y. Chen, F. Wang and X. G. Liu, *J. Am. Chem. Soc.*, 2012, **134**, 20849.
47 B. Zhou, W. F. Yang, S. Y. Han, Q. Sun and X. G. Liu, *Adv. Mater.*, 2015, **27**, 6208.
48 B. Zhou, L. Yan, L. L. Tao, N. Song, M. Wu, T. Wang and Q. Y. Zhang, *Adv. Sci.*, 2018, **5**, 1700667.
49 F. Vetrone, R. Naccache, V. Mahalingam, C. G. Morgan and J. A. Capobianco, *Adv. Funct. Mater.*, 2009, **19**, 2924.
50 F. T. Rabouw, P. T. Prins, P. V. Delgado, M. Castelijns, R. G. Geitenbeek and A. Meijerink, *ACS Nano*, 2018, **12**, 4812.
51 D. Q. Chen, S. Liu, X. Y. Li, S. Yuan and P. Huang, *J. Eur. Ceram. Soc.*, 2017, **37**, 4939.
52 N. J. J. Johnson, S. He, S. Diao, E. M. Chan, H. J. Dai and A. Almutairi, *J. Am. Chem. Soc.*, 2017, **139**, 3275.
53 Q. Q. Li, X. D. Li, L. Zhang, J. Zuo, Y. L. Zhang, X. M. Liu, L. P. Tu, B. Xue, Y. L. Chang and X. G. Kong, *Nanoscale*, 2018, **10**, 12356.
54 Y. F. Shang, S. W. Hao, W. Q. Lv, T. Chen, L. Tian, Z. T. Lei and C. H. Yang, *J. Mater. Chem. C*, 2018, **6**, 3869.
55 A. Pandey, V. K. Rai, V. Kumar and H. C. Swart, *Sens. Actuators, B*, 2015, **209**, 352.
56 B. Dong, B. S. Cao, Y. Y. He, Z. Liu, Z. P. Li and Z. Q. Feng, *Adv. Mater.*, 2012, **24**, 1987.
57 X. Liu and Y. L. Dang, *Sci. Rep.*, 2015, **5**, 15235.

58 F. W. Kang, J. J. He, T. Y. Sun, Z. Y. Bao, F. Wang and D. Y. Lei, *Adv. Funct. Mater.*, 2017, **27**, 1701842.
59 J. J. He, W. Zheng, F. Ligmajer, C. F. Chan, Z. Y. Bao, K. L. Wong, X. Y. Chen, J. H. Hao, J. Y. Dai, S. F. Yu and D. Y. Lei, *Light: Sci. Appl.*, 2016, **6**, e16217.
60 L. Marciniak, K. Prorok and A. Bednarkiewicz, *J. Mater. Chem. C*, 2017, **5**, 7890.
61 Q. P. Qiang, S. S. Du, X. L. Ma, W. B. Chen, G. Y. Zhang and Y. H. Wang, *Dalton Trans.*, 2018, **47**, 8656.
62 L. Marciniak, L. F. Soriano, J. P. Prieto and A. Bednarkiewicz, *Nanoscale*, 2016, **8**, 5037.
63 Z. Y. Sun, J. X. Yang, L. W. Huai, W. X. Wang, Z. D. Ma, J. K. Sang, J. C. Zhang, H. H. Li, Z. P. Ci and Y. H. Wang, *ACS Appl. Mater. Interfaces*, 2018, **10**, 21451.